Generation of matter waves in Bose-Bose mixtures with helicoidal spin-orbit coupling

Conrad Bertrand Tabi, Saravana Veni, and Timoléon Crépin Kofané

Phys. Rev. A **104**, 033325 — Published 29 September 2021

DOI: 10.1103/PhysRevA.104.033325

Generation of matter-waves in Bose-Bose mixtures with helicoidal spin-orbit coupling

Conrad Bertrand Tabi,[1,*] Saravana Veni,[2,†] and Timoléon Crépin Kofané[1,3,4,‡]

[1] *Department of Physics and Astronomy, Botswana International University of Science and Technology, Private Mail Bag 16 Palapye, Botswana*
[2] *Department of Physics, Amrita Institute of Engineering and Technology, Nagercoil - 629 001, India*
[3] *Laboratory of Mechanics, Department of Physics, Faculty of Science, University of Yaoundé I, P.O. Box 812, Yaoundé, Cameroon*
[4] *Centre d'Excellence Africain en Technologies de l'Information et de la Communication, University of Yaoundé I, Cameroon*

(Dated: September 16, 2021)

The paper studies the modulational instability (MI), both theoretically and numerically, of the helicoidal spin-orbit coupled Bose-Bose mixture. An expression of the MI growth rate is found through the linear stability analysis of continuous-wave, followed by a comprehensive parametric study of the MI regions, emphasizing the effects of the spin-orbit coupling, the helicoidal gauge potential, and interatomic interactions. Direct numerical simulations concur with the analytical predictions. Under suitable balance between nonlinear and dispersive effects, trains of soliton-like objects are obtained, and their behaviors are very sensitive to parameter variations. Attention is particularly paid to the impact of the left- and right-handed helicoidal spin-orbit couplings on the appearance of matter-waves that have the form soliton-molecules in the Bose-Bose mixture. Additionally, for qualitative support of the obtained structures, the formation of bright solitons train is also reported numerically using two-neighboring soliton subjected to a fixed phase difference. Their behavior under the action of the helicoidal spin-orbit coupling is also debated, especially when left- and right-handed helicoidal couplings are interchanged.

I. INTRODUCTION

Nonlinear excitations occur ubiquitously in numerous practical and fundamental problems in areas as diverse as nonlinear optics [1], hydrodynamics [2], quantum field theory [3], plasmas [4–6], molecular biology [7–9] and ultracold gases [10]. In general, nonlinear excitations, and solitons in particular, appear due to the interplay between nonlinear and dispersive effects under a universal mechanism known as modulational instability (MI). MI takes place when a constant-wave background becomes unstable by breaking up into sinusoidal modulations, which, to some extent, have soliton-like structures beyond a critical wavenumber. Initially noticed in hydrodynamics, for sinusoidal surface gravity waves in deep water (Stokes waves) by Benjamin and Feir [11], MI was also predicted in optics by Ostrovskii [12] and later by Hasegawa et al. [13] in the optical fiber. Recently, MI has been shown in electrical transmission lines [14, 15], in metamaterials [16], and in biophysical systems such as DNA [17], neural networks [18, 19] and blood vessels [20, 21], just to cite a few. Commonly, it has been noticed that instability can occur in both spatial and temporal domains [22, 23]. Over the past decades, the concept of MI has been broadly extended to one- and two-component Bose-Einstein condensates, where the Gross-Pitaevskii equation (GP) equation has been modified and improved to suitably describe and characterize the occurrence of matter-waves. If in the context of the single-component Bose-Einstein condensate MI was found possible only in the presence of attractive atomic interactions, it was revealed that it might happen in two-component Bose-Einstein condensates even when repulsive interactions are considered within the mean-field (MF) theory. Interestingly, as proposed by Petrov [24], binary Bose-Einstein condensates with competing intra- and inter-component MF interactions of opposite signs offer a platform for the generation of quantum droplets under harmonious interplay between MF dynamics and beyond mean-field (BMF) quantum fluctuations. One of the most important features of all ultradilute quantum systems is the stabilizing role of quantum fluctuations which is crucial in providing self-binding [25–28], manifested by the celebrated Lee-Huang-Yang (LHY) term [26, 29]. The later effect comes into play when the mean-field energy is about to vanish, thus providing energy from the quantum fluctuations so that stable droplets can be formed, in the absence of external trapping, similarly to the case of helium droplets [30, 31]. For instance, the droplets were first produced in Bose gases with dipolar interactions [32–34] and were later extended to binary bosonic mixtures with contact-like interactions [25, 35, 36]. Both in three-dimensional and quasi-one-dimensional systems, two internal states of ^{39}K were recently utilized to realize experiments involving binary mixtures [32, 37, 38]. The formation of self-organized droplet crystals on a hydrophobic surface, beyond a critical magnetization [39–41], was also reported recently as induced by Rosensweig instability in the dipolar condensate of ^{164}Dy for classical ferrofluid. Contrarily, in quantum ferrofluids, self-organized patterns of Rosensweig instability may emerge due to spontaneous symmetry breaking.

* tabic@biust.ac.bw
† s_saravanaveni@amrita.edu.in
‡ tckofane@yahoo.com

Depending on the physical system under consideration, it is evident that the dynamics and stability of quantum droplets are tributaries not only to their mechanism of production but also to the interatomic interactions involved along with the dimension of the mixture. For example, as said earlier, an MF collapsing three-dimensional mixtures, with repulsive intracomponent and attractive intercomponent interactions, is stabilized by including BMF effects [24]. In contrast, in a strictly one-dimensional Bose-Bose (BB) mixture, the BMF attractive energy stabilizes a repulsive MF term [42]. Moreover, it was recently demonstrated the fact that introducing the spin-orbit (SO) coupling could stabilize the quantum droplets, which was confirmed by cold-atom experiments using one-dimensional [43–46] and two-dimensional [47, 48] types of SO coupling. Taking advantage of both the adjustability of the SO coupling and the intrinsic nonlinearity related to interatomic interactions, there has been an increasing interest in studying soliton dynamics and their response to SO coupling effects. Along the same line, the MI of two-component Bose-Einstein condensates under SO coupling effect in one and two dimensions was recently investigated [49, 50]. On that note, the simultaneous effects of SO coupling and Rabi coupling have been addressed explicitly under the activation of MI in Bose-Einstein condensates [49–51]. SO coupling has allowed predicting new types of solitons and nonlinear structures, including half-vortex gap solitons [52], and many other types of discrete and continuum composite solitons [53]. On the other hand, contributions devoted to BB mixtures report the existence of various kinds of localized solitons under the simultaneous action of SO coupling and Rabi coupling [54]. This study was recently extended to characterize quantum droplets via MI [55]. Propagation of solitons in the Bose-Einstein condensates with inhomogeneous helicoidal SO coupling was addressed by Kartashov and Konotop [56]. They were inspired by the fact that light propagation in helical waveguide arrays can generate an artificial helicoidal gauge potential [57], as initially elaborated by Lin et al. [43] who successfully coupled artificial external gauge potentials to neutral cold atoms. The same concept was recently adopted by Li et al. [58], and then by Otlaadisa et al. [59], who respectively investigated the MI, and its response to helicoidal gauge potential and SO coupling, in the vector GP equations and complex Ginzburg-Landau equations. In both contexts, the helicoidal gauge potential was found to break the MI symmetry, strongly impacting the subsequent patterns of instability regions and growth rate in the underlying parameter space. It is our intention, in the present work, to study the characteristics of the MI for the continuous wave (cw) states in helicoidal SO-coupled BB mixtures, which, to the best of our knowledge, entirely remains an open problem. The general methodology relies on confirming results from the linear stability analysis of cws through direct numerical simulations. We show that when system and wave parameters are suitably chosen, symmetry-breaking perturbations appear, which manifest themselves through the emergence of trains of quantum droplets. The appearance of soliton molecules is also explored, and importance is given to their response to the sign of the helicoidal coupling, which can be left- or right-handed. We also give confirmation, via wave-wave interaction, of the close relationship between MI and the appearance of wave trains in the BB mixture. Attention is paid to the impact of the SO coupling parameters under different phase-difference contexts.

The rest of the paper is organized as follows. In Sec. II, we introduce the energy functional of the model from which the modified coupled GP equations that describe the two-component helicoidal SO-coupled BB mixture are derived. We also perform the linear stability analysis for cws and the regions of MI are comprehensively discussed with insistence on the impact of the helicoidal gauge potential and the SO coupling. In Sec. III, predictions from the linear stability analysis are confronted to direct numerical simulations of the governing equations using the split-step Fourier transform method. Section IV is devoted to some concluding remarks.

II. HELICOIDALLY SO-COUPLED GP EQUATIONS AND LINEAR STABILITY ANALYSIS

As considered in Refs. [42, 54], a uniform one-dimensional Bose gas is made of two species with equal mass m and uniform number densities $n_1 = |\Psi_l|^2$ and $n_2 = |\Psi_2|^2$, with the BMF energy density given by [42, 54]

$$\begin{aligned}\mathcal{H}_{1D} = &\frac{(\sqrt{g_{11}}|\Psi_1|^2 - \sqrt{g_{22}}|\Psi_2|^2)^2}{2} \\ &+ \frac{g\delta g}{2}(\sqrt{g_{11}}|\Psi_1|^2 + \sqrt{g_{22}}|\Psi_2|^2)^2 \\ &- \frac{2\sqrt{m}}{3\pi\hbar}\left(g_{11}|\Psi_1|^2 + g_{22}|\Psi_2|^2\right)^{3/2},\end{aligned} \tag{1}$$

where Ψ_l $(l = 1, 2)$ are the two-component bosonic states, and $\hbar$ is the reduced Planck constant. The intracomponent interaction coefficients g_{11} and g_{22} are repulsive, with $g = \sqrt{g_{11}g_{22}}$ and $\delta g = g + g_{12}$, with g_{12} being the intercomponent interaction coefficient that is negative, which caracterizes attractive interspecies interactions. In order to proceed, following [42, 54], we assume $g_{11} = g_{22} = g$, so that Hamiltonian (1) becomes

$$\begin{aligned}\mathcal{H}_{1D} = &\frac{g}{2}(|\Psi_1|^2 - |\Psi_2|^2)^2 + \frac{\delta g}{2}(|\Psi_1|^2 + |\Psi_2|^2)^2 \\ &- \frac{2\sqrt{m}}{3\pi\hbar}g^{3/2}(|\Psi_1|^2 + |\Psi_2|^2)^{3/2},\end{aligned} \tag{2}$$

In the rest of this work, we adopt the units $m = \hbar = 1$. Additionally, the single-particle Hamiltonian $\mathcal{H}_0$ of the system is given by

$$\mathcal{H}_0 = \frac{[p + \alpha A(x)]^2}{2} + \frac{\Delta\sigma_z}{2}, \tag{3}$$

with $p = -i\partial/\partial x$ being the linear momentum operator. $A(x)$ is the spatially varying gauge potential with amplitude α, while Δ and $\sigma_{x,y,z}$ are, respectively, the Zeeman splitting and Pauli matrices. This leads to the energy functional for the BB mixture which is such that

$$\mathcal{E} = \int_{-\infty}^{+\infty} dx[\mathcal{H}_{1D}(|\Psi_1|^2, |\Psi_2|^2) + \Psi^\dagger \mathcal{H}_0 \Psi], \quad (4)$$

where $\Psi = (\Psi_1, \Psi_2)^T$. Following the procedure introduced in Ref. [56] and further used in [58, 59], a gauge transformation,

$$\Psi = e^{-i(\alpha^2+\beta^2)t/2} e^{-i\sigma_z \beta x} \psi, \quad (5)$$

is adopted to switch to the rotating frame for the chosen gauge field $A(x)$. Therefore, the different components of the BB mixture are described by the generalized GP equations:

$$\begin{aligned} i\frac{\partial \psi_l}{\partial t} = & -\frac{1}{2}\frac{\partial^2 \psi_l}{\partial x^2} - (-1)^l i\beta \frac{\partial \psi_l}{\partial x} - i\alpha \frac{\partial \psi_{3-l}}{\partial x} - (-1)^l \frac{\Delta}{2}\psi_l \\ & + \frac{\delta g}{2}(|\psi_l|^2 + |\psi_{3-l}|^2)\psi_l - (-1)^l g(|\psi_l|^2 - |\psi_{3-l}|^2)\psi_l \\ & - \frac{g^{3/2}}{\pi}\left(\sqrt{|\psi_l|^2 + |\psi_{3-l}|^2}\right)\psi_l, \quad l = 1, 2. \end{aligned} \quad (6)$$

Precision should be made that the SO coupling, whose strength is experimentally tunable using different techniques, is considered of the helicoidal shape with the period π/β, which explicitly means that the helicoidal structure of the vector potential is point translational symmetry, where β is the frequency of rotation, also addressed as the helicoidal gauge potential, with the positive and negative values of β, respectively, characterizing the right-handed and left-handed modes [60, 61].

The MI of the set of Eqs.(6) can be studied through the linear stability analysis of cws. This is done by considering a mixture with uniform densities $n_{10} = n_{20} = n_0$, and a uniform chemical potential μ for both components. The corresponding cw states are written in the form

$$\psi_l = e^{-i\mu t}\sqrt{n_0}, \quad l = 1, 2, \quad (7)$$

where the Zeeman splitting, the interatomic interactions and chemical potential are related by the equation

$$\Delta = -2(-1)^l \left(\mu + \frac{\sqrt{2}}{\pi} g^{3/2}\sqrt{n_0} - \delta g n_0\right) \quad (8)$$

obtained by introducing solution (7) into Eqs.(6). We should also stress that the chemical potential μ represents the fundamental frequency of the Bogoliubov excitation spectrum [62, 63], and therefore represents the condition for the cws (7) to be solution of Eqs.(6). Moreover, the stability of the cws is tested by introducing small perturbations $a_l(x,t)$ $(l = 1, 2)$, with $|a_l(x,t)| \ll \sqrt{n_0}$, so that

$$\psi_l = e^{-i\mu t}(\sqrt{n_0} + a_l(x,t)). \quad (9)$$

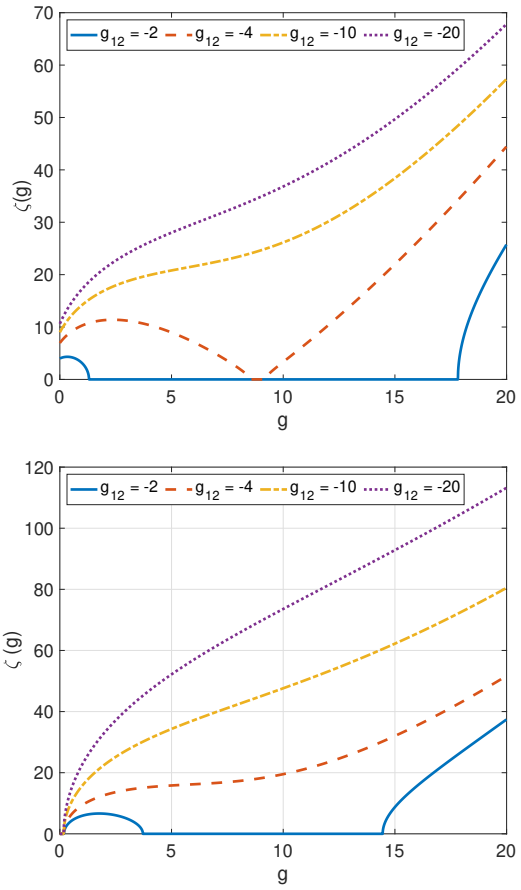

Figure 1. (Color online) Distribution of the MI growth rate versus the intracomponent coupling strength g for different values of the intercomponent interaction strength g_{12}, with (a) $\beta = 0$, $\alpha = 0$, (b) $\beta = 1$, and $\alpha = 0.5$, $K = 2$ and $n_0 = 1$.

Substituting Eq. (9) into Eqs. (6), and linearizing around the unperturbed cws lead to the following Bogoliubov-de Gennes equations in terms of a_l $(l = 1, 2)$:

$$\begin{aligned} i\frac{\partial a_1}{\partial t} = & -\frac{1}{2}\frac{\partial^2 a_1}{\partial x^2} + i\beta\frac{\partial a_1}{\partial x} - i\alpha\frac{\partial a_2}{\partial x} \\ & + \left(\left(\frac{\delta g}{2} + g\right)n_0 - \frac{g^{3/2}}{2\sqrt{2}\pi}\sqrt{n_0}\right)(a_1 + a_1^*) \\ & + \left(\left(\frac{\delta g}{2} - g\right)n_0 - \frac{g^{3/2}}{2\sqrt{2}\pi}\sqrt{n_0}\right)(a_2 + a_2^*), \end{aligned} \quad (10a)$$

$$\begin{aligned} i\frac{\partial a_2}{\partial t} = & -\frac{1}{2}\frac{\partial^2 a_2}{\partial x^2} - i\beta\frac{\partial a_2}{\partial x} - i\alpha\frac{\partial a_1}{\partial x} \\ & + \left(\left(\frac{\delta g}{2} - g\right)n_0 - \frac{g^{3/2}}{2\sqrt{2}\pi}\sqrt{n_0}\right)(a_1 + a_1^*) \\ & + \left(\left(\frac{\delta g}{2} + g\right)n_0 - \frac{g^{3/2}}{2\sqrt{2}\pi}\sqrt{n_0}\right)(a_2 + a_2^*), \end{aligned} \quad (10b)$$

where a_l^* are the complex conjugates of the perturbed fields a_l. We further assume the following trial solutions

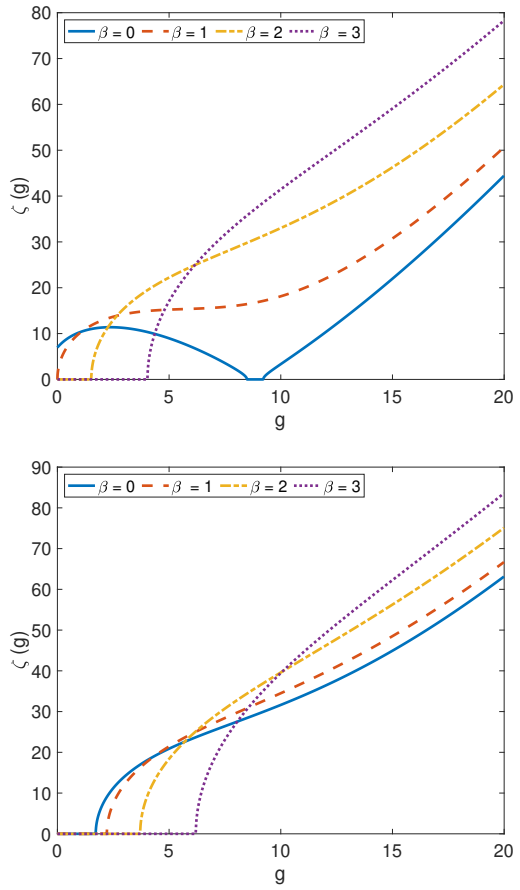

Figure 2. (Color online) Plots of the maximum instability growth rate versus the intracomponent coupling strength g for $\alpha = 0$ [panel (a)] and $\alpha = 2$ [panel (b)], when β takes different values. The other parameters are: $K = 2$, $g_{12} = -4$, and $n_0 = 1$.

for the perturbed field equations:

$$a_l(x,t) = \zeta_l \cos(Kx - \Omega t) + i\eta_l \sin(Kx - \Omega t), \tag{11}$$

where K is a real wavenumber, Ω is a complex eigenfrequency, ζ_l and η_l are real amplitudes that are obtained by solving the following set of homogeneous equations:

$$\mathbf{M} \times (\eta_1, \zeta_1, \eta_2, \zeta_2)^T = 0, \tag{12}$$

where $\mathbf{M}$ is a 4×4 matrix given by

$$\mathbf{M} = \begin{pmatrix} \Omega + n_{11} & n_{12} & n_{13} & n_{14} \\ n_{21} & \Omega + n_{22} & n_{23} & n_{24} \\ n_{31} & n_{32} & \Omega - n_{33} & n_{34} \\ n_{41} & n_{42} & n_{43} & \Omega - n_{44} \end{pmatrix}, \tag{13}$$

and whose elements are given by

$$\begin{aligned}
&n_{11} = n_{22} = n_{33} = n_{44} = \beta K, \\
&n_{12} = -\frac{K^2}{2}, \; n_{13} = -\alpha K, \;\; n_{14} = 0, \\
&n_{21} = -\frac{1}{2}\left(K^2 + 2n_0(3g + g_{12}) - \frac{2g^{3/2}\sqrt{n_0}}{\pi\sqrt{2}}\right), \\
&n_{23} = -(g_{12} - g)n_0 + \frac{g^{3/2}\sqrt{n_0}}{\pi\sqrt{2}}, \\
&n_{24} = n_{13} = n_{31}, \;\; n_{32} = 0, \;\; n_{42} = n_{13}, \\
&n_{34} = n_{12}, \;\; n_{41} = -(g_{12} - g)n_0 + \frac{g^{3/2}\sqrt{n_0}}{\pi\sqrt{2}}, \\
&n_{43} = -\frac{1}{2}\left(K^2 + 2n_0(3g + g_{12}) - \frac{2g^{3/2}\sqrt{n_0}}{\pi\sqrt{2}}\right).
\end{aligned} \tag{14}$$

System (12) will admit nontrivial solutions if its determinant is null, i.e., $\det(\mathbf{M}) = 0$, which leads, after some straightforward calculations, to the nonlinear dispersion relation

$$\Omega^4 + P_2\Omega^2 + P_1\Omega + P_0 = 0, \tag{15}$$

with the coefficients $P_l (l = 0, 1, 2)$ being given by

$$\begin{aligned}
P_2 &= \frac{K^2}{2\pi}(-\sqrt{2n_0}g^{3/2} + 2\pi\,(3g + g_{12})\,n_0 \\
&\quad + \pi\left(4\left(\alpha^2 + \beta^2\right) + K^2\right)), \\
P_1 &= \frac{\sqrt{2n_0}\alpha g^{3/2}K^3}{\pi} + 2\alpha n_0\,(g - g_{12})\,K^3, \\
P_0 &= \frac{K^4}{16\pi}\left(-4\left(\alpha^2 + \beta^2\right) + 8gn_0 + K^2\right) \\
&\quad \times (-2\sqrt{2}g^{3/2}\sqrt{n_0} + 4\pi\,(g + g_{12})\,n_0 \\
&\quad + \pi\left(K^2 - 4\left(\alpha^2 + \beta^2\right)\right)).
\end{aligned} \tag{16}$$

Moreover, Eq.(15) can be solved to obtain the following four solutions:

$$\begin{aligned}
\Omega_{1,2} &= -\frac{1}{2}\sqrt{\Lambda - \frac{2}{3}P_2} \\
&\quad \pm \frac{1}{2}\sqrt{-\frac{4}{3}P_2 - \Lambda + \frac{8P_0}{4\sqrt{-\frac{2}{3}P_2 + \Lambda}}}, \\
\Omega_{3,4} &= \frac{1}{2}\sqrt{\Lambda - \frac{2}{3}P_2} \\
&\quad \pm \frac{1}{2}\sqrt{-\frac{4}{3}P_2 - \Lambda - \frac{8P_0}{4\sqrt{-\frac{2}{3}P_2 + \Lambda}}},
\end{aligned} \tag{17}$$

where $\Lambda = \frac{1}{3}\left(\sqrt[3]{\frac{\Delta_2 + \sqrt{\Delta_2^2 - 4\Delta_1^3}}{2}} + \frac{\Delta_1}{\sqrt[3]{\frac{\Delta_2 + \sqrt{\Delta_2^2 - 4\Delta_1^3}}{2}}}\right)$, and $\Delta_1 = P_2^2 + 12P_0$, $\Delta_2 = 2P_2^3 + 27P_1^2 - 72P_2P_0$. The set

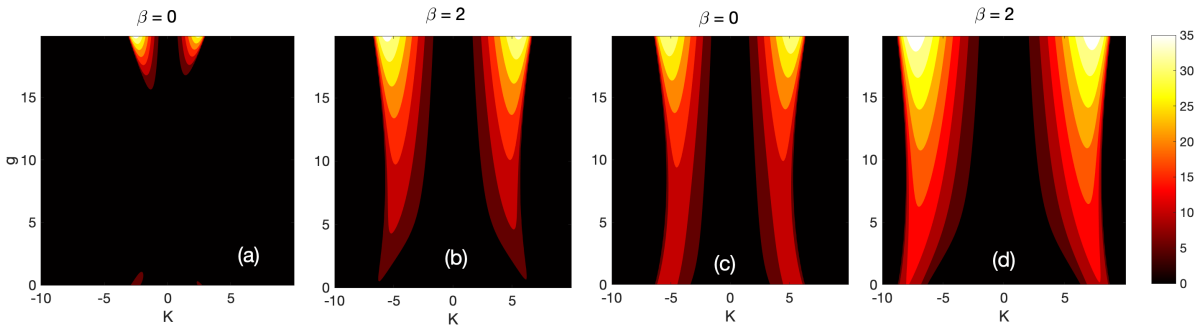

Figure 3. (Color online) Distribution of the instability growth rate in the $(K, g)-$plane when the intracomponent interaction strength g_{12} takes the values: (a)-(b) $g_{12} = -2$ and (c)-(d) $g_{12} = -10$, with $\alpha = 0.5$, $K = 2$, $n_0 = 1$ and β taking values 0 and 2 for each of the cases.

of solutions (17) implies that Ω may be positive, negative or even complex, depending on the system parameters. However, real, negative or positive, values of Ω predict the stability of the cws. General complex solutions of Eq.(15) are such that $\Omega = \Omega_r + i\Omega_i$, so that $e^{-i\Omega t} = e^{-i\Omega_r t} \times e^{\Omega_i t}$. This means that the occurrence of instability fully depends on the imaginary part of the perturbation frequency and necessary information on the onset of MI can be extracted through the maximum growth rate given by

$$\zeta(\Omega) = \{|\mathrm{Im}(\Omega)|\}_{max}. \tag{18}$$

Interestingly, the MI growth rate depends on parameters g, g_{12} and the newly introduced helicoidal and spin-orbit parameters α and β. Nevertheless, the reader can notice that the Zeeman effect is not included in the expression of the coefficients P_l, so it will not affect the growth rate.

As we have introduced the helicoidal gauge potential and the SO coupling terms, values of interatomic interactions giving rise to MI may likely change. To solve that problem, we introduce the analysis here by finding regions of positive growth rate that may support the disintegration of cws. It is, however, of importance to first consider the case that does not include β and α, which is depicted in Fig.1(a), where ζ is represented versus the intracomponent coupling strength g, with changing the intercomponent interaction parameter g_{12}. Obviously, for the latter decreasing, the growth rate gets modified, and regions admitting MI get expanded. For $g_{12} = -2$, one notices a large zone of forbidden values of g. At the same time, regions of instability are situated at the edges of the allocated interval, which otherwise means that only small values and high values of g may give rise to MI. The gap reduces for $g_{12} = -4$, and the two instability zones merge for $g_{12} = -10$ and -20. In the presence of the helicoidal gauge potential and the SO coupling terms, i.e., $\alpha \neq 0$ and $\beta \neq 0$, $g_{12} = -2$ gives rise to the same scenario as in Fig.1(a). Still, the marginal instability gets enhanced for $g_{12} < -2$, which means that the presence of the SO coupling and small values of the intercomponent coupling strength contribute to enhance instability [see Fig.1(b)]. Further investigations in the same direction show that the behaviors of MI growth rate are very sensitive to changes in α and β as recorded in Fig. 2. To plot Fig. 2(a), we have fixed $g_{12} = -4$ and $\alpha = 0$, while β was increased from zero. The MI growth rate switches from two regions of instability that merge to form a large region of instability preceded by a forbidden interval of g, where values are not supposed to support the appearance of solitons. This appears when $\beta = 3$. When $\alpha = 2$, with g_{12} keeping the same value as in Fig. 2(a), the results show that the forbidden $g-$values appear even for $\beta = 0$, and get expanded with increasing β, so that there will be no instability for $g < g_{cr}$. g_{cr} is a function of β and can also be influenced by values of α, which bring about the SO coupling effect. This is further confirmed in Fig. 3, where ζ is represented in the $(K, g)-$plane, when g_{12} takes different values, with $\alpha = 0.5$. When $\beta = 0$ and $g_{12} = -2$ [see Fig. 3(a)], high values of the growth rate are obtained for big values of g, while the MI spectrum appears in the form of two asymmetric lobes with respect to $K = 0$. However, for the same values of g_{12}, but $\beta = 2$, the initial two lobes of instability not only expand but also cover all the possible values of g, even though the gap between them gets bigger. The same calculations are repeated for $g_{12} = -10$ and recorded in Figs. 3(c) and (d), respectively for $\beta = 0$ and $\beta = 2$. In the first case, i.e., Fig. 3(c), decreasing the values of g_{12} makes $g = 0$ a possible value that may lead to cw disintegration, and lobes are larger than those of Fig. 3(a) for the same value of β. Also, the ζ intensity decreases with g, a phenomenon that is also ostensible in Fig. 3(d), where $\beta = 2$. The later value of the helicoidal gauge potential affects both the spatial expansion of the instability zone and the forbidden gap for $K-$values. Such features support the fact that the development of MI in the BB mixture is significantly affected by the interatomic interactions. At the same time, richer behaviors are brought by the helicoidal gauge potential and the SO coupling, which requires some comprehensive analysis of their combined effects. This is summarized in Figs. 4-7.

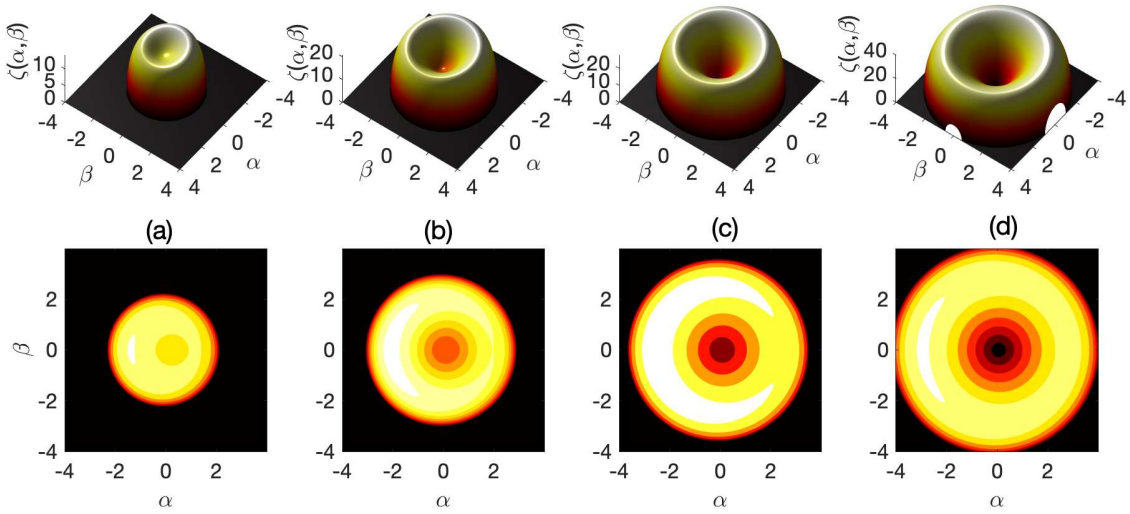

Figure 4. (Color online) Distribution of the instability growth rate in the $(\alpha, \beta)-$plane for $g_{12} = -4$ and: (a) $g = 2$, (b) $g = 4$, (c) $g = 6$, and (d) $g = 8$, with $K = 2$, $n_0 = 1$.

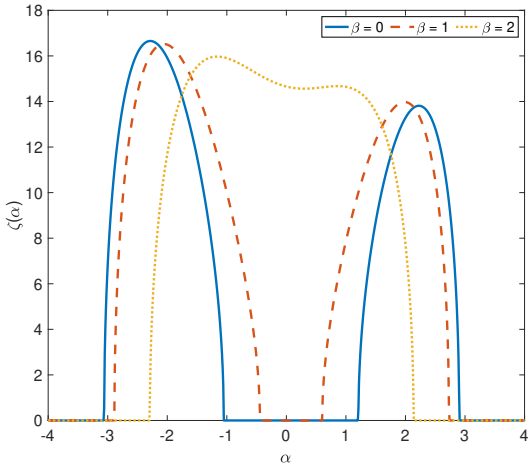

Figure 5. (Color online) Plots of the maximum instability growth rate versus the SO-coupling strength α, for $g = 4$, $g_{12} = -4$, $K = 2$, $n_0 = 1$, $\beta = 0$, $\beta = 1$, and $\beta = 2$.

Different figures of the MI growth rate versus α and β are shown, and one pays particular attention to their response to changes in the intracomponent interactions when g_{12} is fixed. The first example, the one corresponding to $g_{12} = -4$, is illustrated in Fig. 4, where instability is supported by values of α and β distributed throughout a cylindrical MI growth rate. With increasing g, the asymmetric cylinder in α gets expanded, reducing the surrounding area of stability, while a circular zone of decreasing growth rate appears at the center and expands, creating a zone of instability around, and including, $\alpha = \beta = 0$. However, one should stress that the obtained circular MI growth rate is symmetric in the $\beta-$directions and asymmetric in the $\alpha-$direction, which predicts the presence of asymmetric lobes of instability. Therefore, the growth rate may behave the same way for Bose mixtures with right-handed ($\beta < 0$) and left-handed ($\beta > 0$) helicoidal SO couplings. To confirm the asymmetry of ζ in the $\alpha-$direction, the growth rate of MI has been represented in Fig. 5 versus the SO coupling strength α, with $g = 4$ and $g_{12} = -4$. Interestingly, when β increases from 0 to 2, two asymmetric lobes appear. The region of stability between the lobes shrinks until the merging of the two lobes into a single area of instability that remains asymmetric with respect to $\alpha = 0$. On the other hand, with decreasing g_{12} to -20, the same behaviors of MI appear, except that the dome of instability generated by the calculations remains full and the unique regions of stability remain those around the closed cylinder of instability[see Fig. 6]. Such results are additionally supported by the spectrum of behaviors of Fig. 7, where ζ is also represented as a function of α, when $g = 4$ and $g_{12} = -20$. With β changing, the symmetric door of instability expands, reducing possibilities for the cws to remain stable. This also implies that no suitable balance between nonlinear and dispersive effects can be obtained, except in selected regions of parameters as noticed in the above analysis. Indeed, the detected regions just give information about the onset of MI in the Bose mixture but do not unveil any additional details on the longtime evolution of any subsequent nonlinear structure. Answers to such concerns should indubitably be obtained through direct numerical simulations on the generic equations.

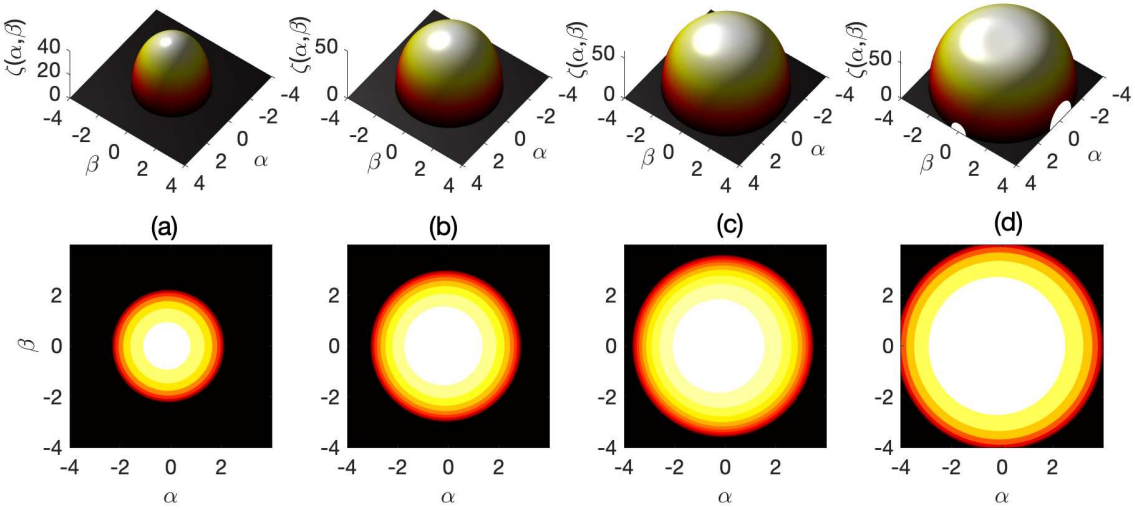

Figure 6. (color online) Distribution of the instability growth rate in the $(\alpha, \beta)-$plane for $g_{12} = -20$ and: (a) $g = 2$, (b) $g = 4$, (c) $g = 6$, and (d) $g = 8$, with $K = 2$, $n_0 = 1$.

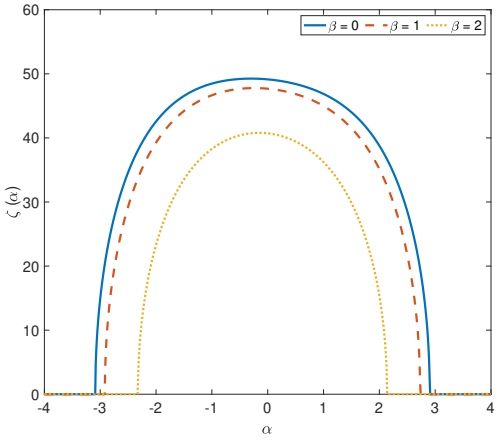

Figure 7. (Color online) Plots of the maximum instability growth rate versus the SO-coupling strength α, for $g = 4$, $g_{12} = -10$, $K = 2$, $n_0 = 1$, with β taking the respective values $\beta = 0$, $\beta = 1$, and $\beta = 2$.

III. NUMERICAL EXPERIMENTS ON CW INSTABILITY

In this section, we confront our analytical predictions to direct numerical simulations on generic equations (6). For that purpose, the the split-step Fourier method, with the initial conditions

$$\psi_1(x, 0) = \psi_2(x, 0) = n_0 + \varepsilon \cos(Kx), \qquad (19)$$

is used. The perturbation wavenumber K takes values from the instability regions of Figs. 1-7, $n_0 = 1$ and $\varepsilon = 0.001$, so that $\varepsilon \ll n_0$. The manifestation of MI is debated through the amplitude maxima, and importance is given to the impact of the helicoidal gauge potential and the SO coupling effect, under different combinations of the interatomic interactions strengths g and g_{12}. In all numerical simulations, we use $\Delta = 0.01$.

Under the above conditions, Fig. 8 shows the spatiotemporal evolution of the perturbed cw densities for the set of parameters $(\alpha = 0, \beta = 0)$ and $(\alpha = 0, \beta = 2)$. In the first case, the choice of the interatomic parameters and the wavenumber creates a competition between nonlinear and dispersive effects, which leads the cws to break into identical spatiotemporal patterns for each component of the mixture [see Fig. 8(a)]. However, the onset of MI is such that there is a time delay before the appearance of the nonlinear structures, which the linear stability analysis has not predicted. Nevertheless, by comparing the maximum amplitudes of such structures, one confirms that they are identical. Still, the density $|\psi_2|^2_{max}$ is higher, while the initial perturbations grow and solitons appear, thus confirming the analytical predictions [see Fig. 8(c1)]. Interestingly, the dynamics changes when we switch on the helicoidal gauge potential, leaving the SO coupling strength to zero [see Fig. 8(b)]. At first sight, the coherent states of Fig. 8(a) get destroyed, but solitons remain robust in the mixture. At the same time, their appearance experiences a time delay, which does not change the maximum amplitude of the component ψ_2 which remains higher [see Fig. 8(c2)]. Precision should be made that we have fixed $g = 2$ and $g_{12} = -4$, which implies that the intercomponent interactions are attractive, while the intracomponent interactions are repulsive. That choice of parameters was indeed found to support the appearance of solitons, which corroborates our numerical findings.

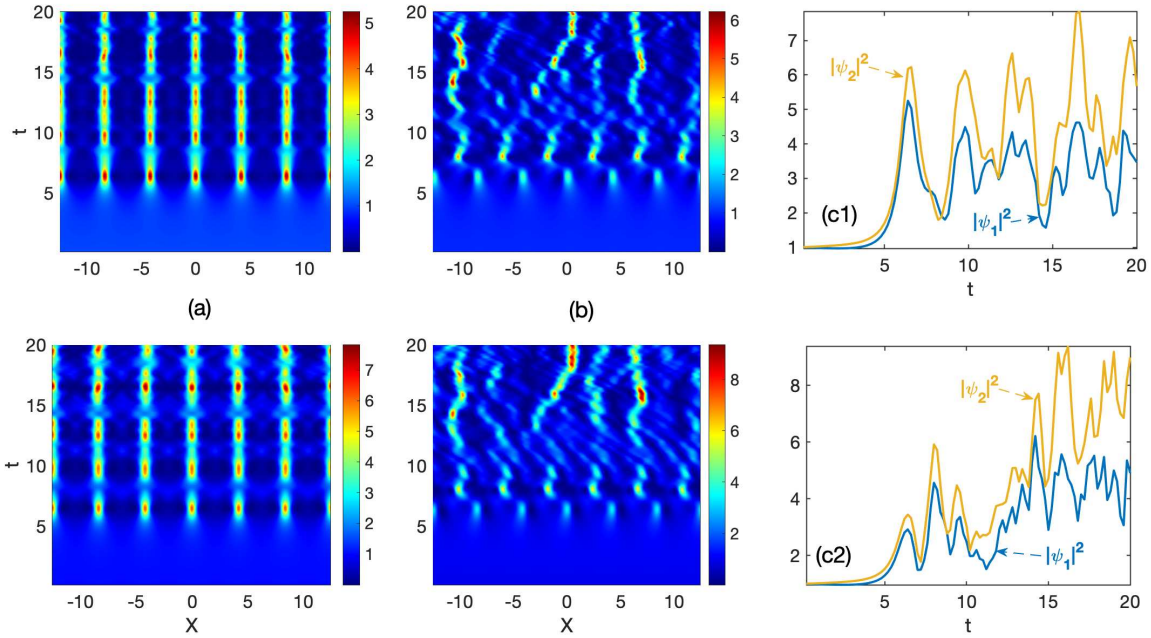

Figure 8. (Color online) (a) and (b): Spatiotemporal evolution of the mixture densities as a consequence of development of MI for $\alpha = 0$, $\beta = 0$ (panels (a)), $\alpha = 0$, $\beta = 1$ (panels(b)), where the upper line gives $|\psi_1|^2$ and the bottom line depicts $|\psi_2|^2$. Panel (cj)$_{j=1,2}$ compare the time evolution of $|\psi_1|^2_{max}$ (blue line) and $|\psi_2|^2_{max}$ (yellow line). (c1) corresponds to $\alpha = 0$, $\beta = 0$ and (c2) gives results for $\alpha = 0$, $\beta = 1$. The rest of the parameters are: $g = 2$, $g_{12} = -4$, $K = 1.5$ and $n_0 = 1$.

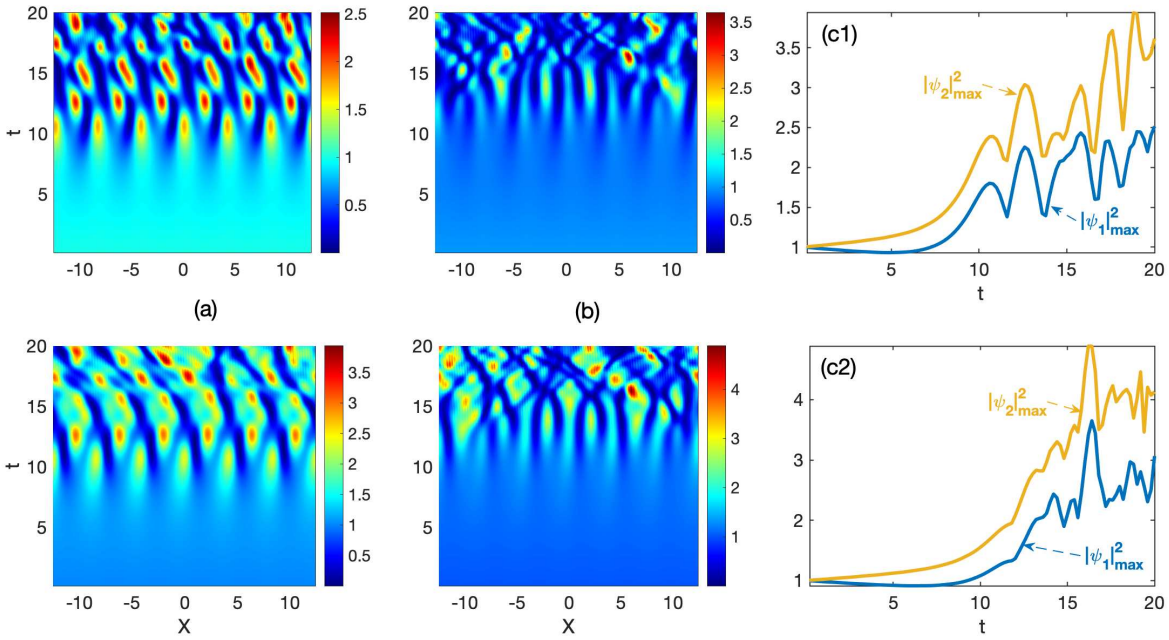

Figure 9. (Color online) (a) and (b): Spatiotemporal evolution of the mixture densities as a consequence of development of MI for $\alpha = 0.5$, $\beta = 0$ (panels (a)), $\alpha = 0.5$, $\beta = 1$ (panels(b)), where the upper line gives $|\psi_1|^2$ and the bottom line depicts $|\psi_2|^2$. Panel (cj)$_{j=1,2}$ compare the time evolution of $|\psi_1|^2_{max}$ (blue line) and $|\psi_2|^2_{max}$ (yellow line). (c1) corresponds to $\alpha = 0.5$, $\beta = 0$ and (c2) gives results for $\alpha = 0.5$, $\beta = 1$. The rest of the parameters are: $g = 2$, $g_{12} = -4$, $K = 1.5$ and $n_0 = 1$.

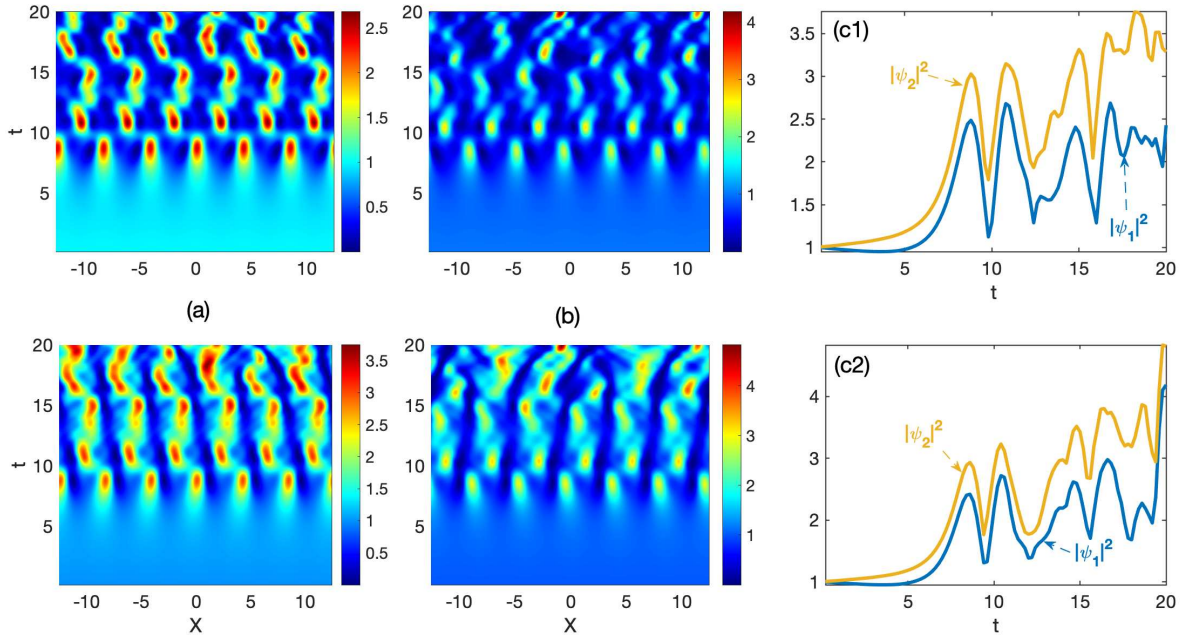

Figure 10. (Color online) (a) and (b): Spatiotemporal evolution of the mixture densities as a consequence of development of MI for $\alpha = 0.05$, $\beta = 1$ (panels (a)), $\alpha = 0.05$, $\beta = -1$ (panels(b)), where the upper line gives $|\psi_1|^2$ and the bottom line depicts $|\psi_2|^2$. Panel (cj)$_{j=1,2}$ compare the time evolution of $|\psi_1|^2_{max}$ (blue line) and $|\psi_2|^2_{max}$ (yellow line). (c1) corresponds to $\alpha = 0.05$, $\beta = 1$ and (c2) gives results for $\alpha = 0.05$, $\beta = -1$. The rest of the parameters are: $g = 2$, $g_{12} = -4$, $K = 1.5$ and $n_0 = 1$.

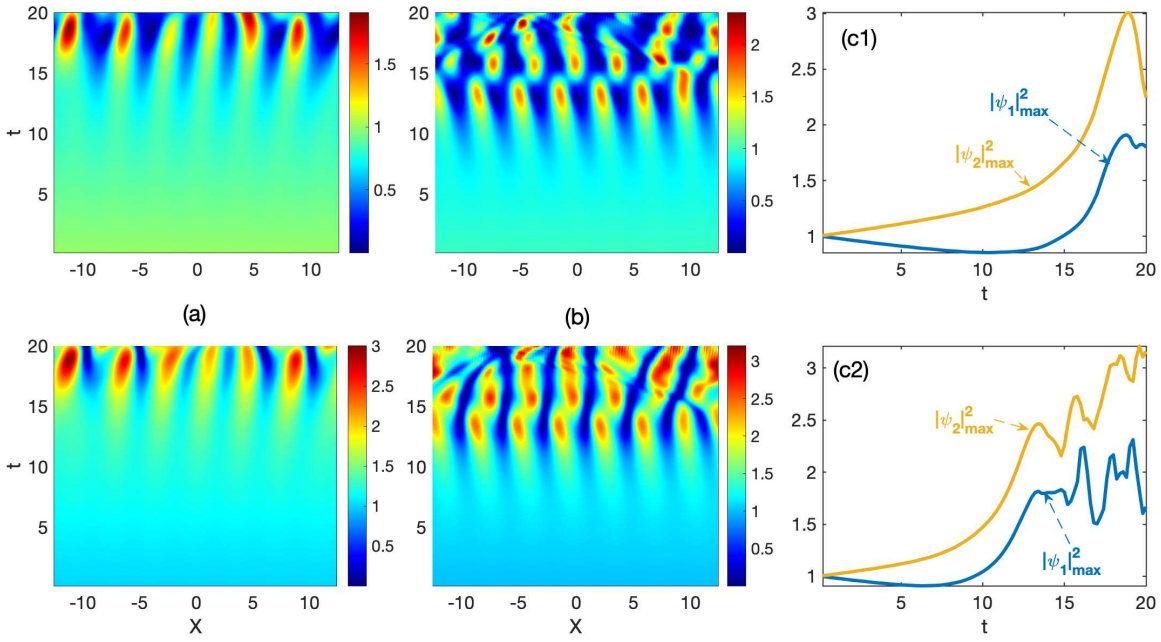

Figure 11. (Color online) (a) and (b): Spatiotemporal evolution of the mixture densities as a consequence of development of MI for $\alpha = 0.75$, $\beta = 1$ (panels (a)), $\alpha = 0.75$, $\beta = -1$ (panels(b)), where the upper line gives $|\psi_1|^2$ and the bottom line depicts $|\psi_2|^2$. Panel (cj)$_{j=1,2}$ compare the time evolution of $|\psi_1|^2_{max}$ (blue line) and $|\psi_2|^2_{max}$ (yellow line). (c1) corresponds to $\alpha = 0.75$, $\beta = 1$ and (c2) gives results for $\alpha = 0.75$, $\beta = -1$. The rest of the parameters are: $g = 2$, $g_{12} = -4$, $K = 1.5$ and $n_0 = 1$.

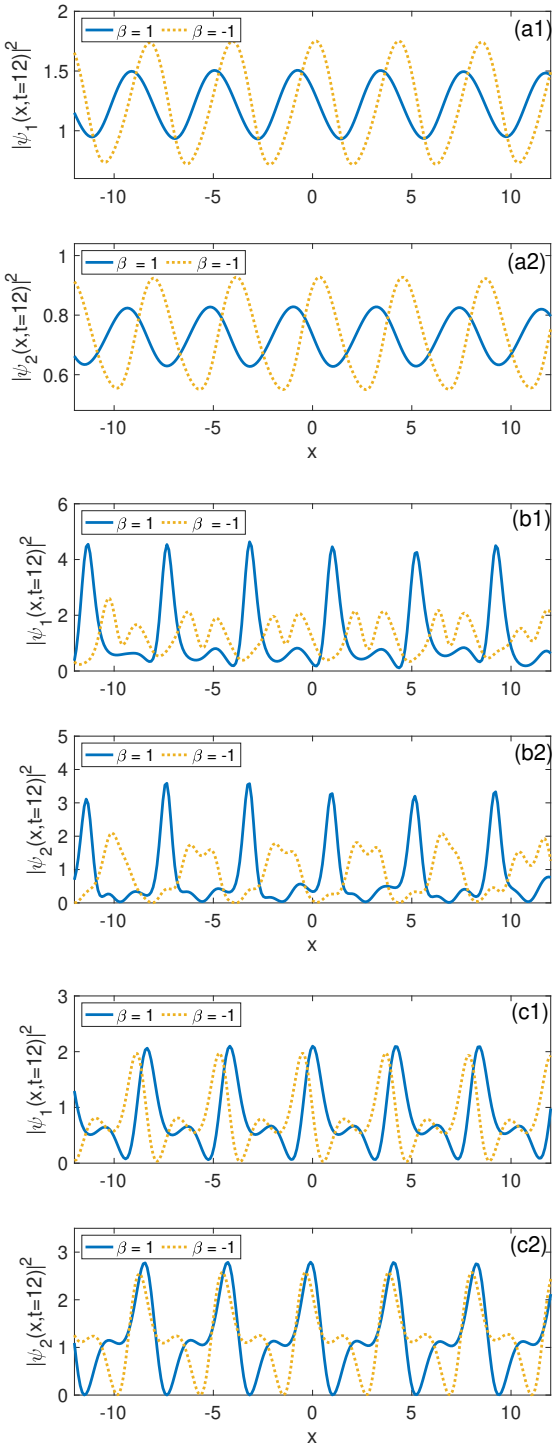

Figure 12. (Color online) Cross sections of the density profiles when $\beta = 1$ (blue line) and $\beta = -1$ (yellow line) for: $(\mathrm{aj})_{j=1,2}$ $\alpha = 0.5$, $g = 2$ and $g_{12} = -2$, $(\mathrm{bj})_{j=1,2}$ $\alpha = 0.5$, $g = 0.5$ and $g_{12} = -2$, $(\mathrm{cj})_{j=1,2}$ $\alpha = 0.5$, $g = 1$ and $g_{12} = -2$. Beyond the stability of the cws, the MI, result of the balance between nonlinear and dispersive effects, is manifested by the appearance of soliton molecules whose topologies change with the sign of the helicoidal gauge potential β.

Keeping the same values for g and g_{12}, we fix $\alpha = 0.5$ and $\beta = 0$ to generate the numerical patterns of Fig. 9(a), which clearly show that the SO coupling can bring about chains of droplet-like states in the Bose mixture. Except for all the other characteristics of the emerging structures, they tend to propagate toward the negative $x-$direction for both components, while the delay before their emergence has increased compared to the results of Fig. 8. This is further confirmed by the manifestations of MI delivered by Fig. 9(c1), where $|\psi_1|^2_{max}$ and $|\psi_2|^2_{max}$ are compared. Moreover, as expected from the results of Fig. 8(b), erratic patterns appear in Fig. 9(b), where α keeps the same value, and β is attributed the value 1. Although the time delay for wave patterns to appear has further increased, the MI phenomenon persists, but the wave train deviation to the negative $x-$direction has disappeared. One may also notice an increase in the densities of Fig. 9(b), which implies that the direct action of the helicoidal gauge potential, in this case, destabilizes the mixture and, more importantly, modifies the trail of droplet-like chains, and favors energy exchange to boost the magnitude of lower densities. This aspect is also supported by the instability figures summarized in Fig. 9(c2).

In the parametric study of the linear stability of cws, it was revealed that the growth rate was symmetric for the helicoidal gauge potential, in the left- and right-handed contexts. However, it was obtained in Refs. [58, 59] that the instability and the longtime evolution of subsequent patterns can be highly affected by the sign of β. This is further confirmed in the present contribution as summarized in Fig. 10, for which $g = 2$, $g_{12} = -1.8$ and $\alpha = 0.05$. Fig. 10(a) corresponds to $\beta = 1$, while Fig. 10(b) has been generated for $\beta = -1$. In all the cases, trains of droplet-like waves are triggered after a quiescent period, but the structures are more coherent for $\beta > 0$. However, for $\beta < 0$, the densities are high for both components, while the spatiotemporal expansion on the individual elements of the trains drops. The maxima of their amplitudes present identical dynamics at the early stage of instability, but each component oscillates differently after a certain period of time. Further calculations show that with increasing α to 0.75, the competition between the SO coupling and the gauge potential reveals more fascinating features as shown in Fig. 11. For the left-handed gauge potential, i.e., $\beta > 0$, the time needed for MI to appear is high than when $\beta < 0$, which refers to the right-handed gauge potential [see Fig. 11(b)]. This is clearly supported by the maximum modulus squares $|\psi_1|^2_{max}$ and $|\psi_2|^2_{max}$ of Figs. 11(c1) and (c2). In order to observe this phenomenon more clearly, the cross-sections of the density profiles for the two components of the BB mixtures are compared in Fig. 12.

The panels $(\mathrm{aj})_{j=1,2}$ of Fig. 12 show the behaviors of stable cws obtained for $\alpha = 0.5$, $g = 2$ and $g_{12} = -2$. For left- and right-handed helicoidal couplings, the cws remain stable even though the change in the sign of β affects their amplitudes. The effect of the sign of β is further studied by considering regions of parameters ca-

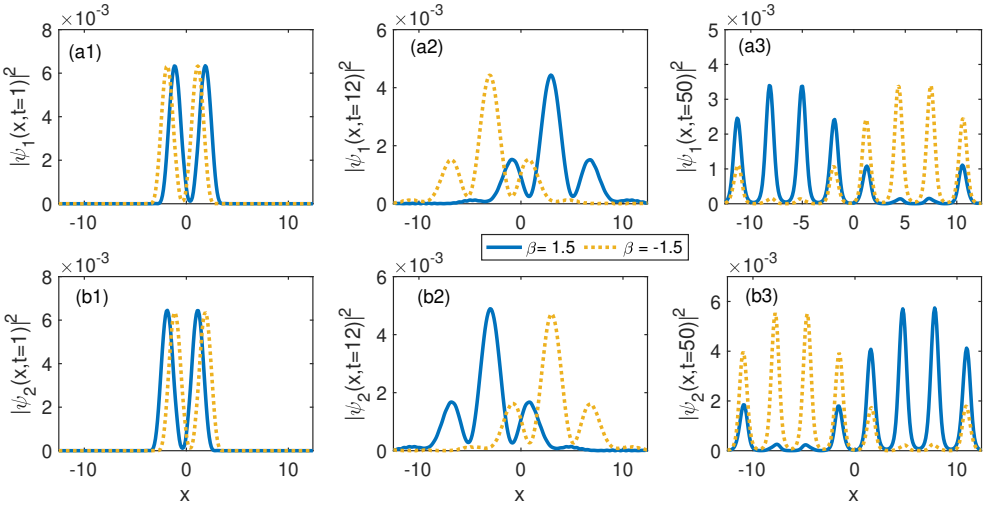

Figure 13. (Color online) The panels display soliton train formation due to two neighboring bright solitons with phase difference $\Delta\phi = 0$, at different instants $t = 1$, $t = 12$ and $t = 50$. Fixing $\alpha = 0.5$, $g = 0.5$ and $g_{12} = -1.25$, it is obvious that the density profiles are switched when the sign of the helicoidal gauge potential β changes.

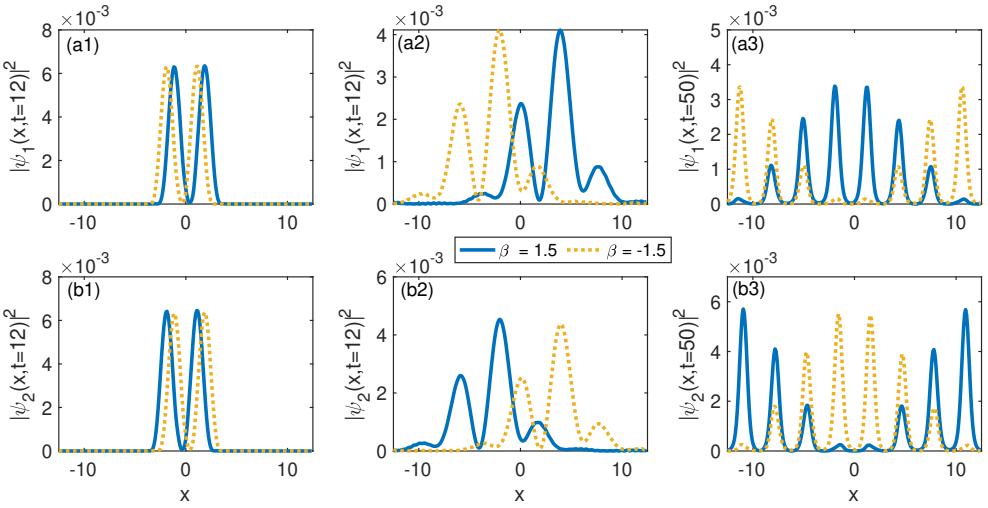

Figure 14. (Color online) The panels display soliton train formation due to two neighboring bright solitons with phase difference $\Delta\phi = \pi/2$, at different instants $t = 1$, $t = 12$ and $t = 50$. Fixing $\alpha = 0.5$, $g = 0.5$ and $g_{12} = -1.25$, it is obvious that the density profiles are switched when the sign of the helicoidal gauge potential β changes.

pable of giving rise to nonlinear structures. We then fix $g = 0.5$ and $g_{12} = -2$ to obtain the features of Fig. 12(bj)$_{j=1,2}$ which correspond to trains of coupled solitonic objects. This latter observation brings, once more, forth the fact that the MI is a direct mechanism capable of leading to the formation of any class/category of wave structures. Otherwise, the suitable balance between nonlinear and dispersive effects is also capable of inducing what is called *soliton molecules* [64–66]. In general, soliton molecules are related to double-hump intensity profiles made of two solitons. Their temporal version has been reported in nonlinear optics, via the generalized and the dissipative NLS equations [67–69] and the complex Ginzburg-Landau equation [70, 71]. Figs. 12(cj)$_{j=1,2}$ present an intriguing phenomenon related to the change in the sign of β, for $g = 1$ and $g_{12} = -2$, with α and K keeping the same values. In fact, each molecule of the wave train is made of two asymmetric structures. The resulting composite soliton was already reported in Ref. [72], in SO coupled spin-1 condensates, as emerging from colliding vector solitons. In Figs. 12(c1) and (c2), one clearly notices that the lower hump of the molecule changes side when the sign of the helicoidal gauge potential changes, which once more justifies the importance of the effectiveness of the helicoidal SO coupling in the studied model. This also demonstrates the important

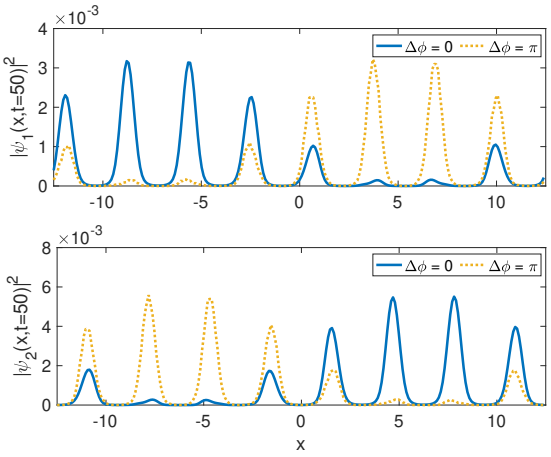

Figure 15. (Color online) The panels display soliton train formation due to two neighboring bright solitons. The emerging interferences due to the difference $\Delta\phi = 0$ (blue solid line) and difference $\Delta\phi = \pi$ (dotted yellow line) are compared at time $t = 50$. We have fixed $\alpha = 0.25$, $\beta = 1.75$, $g = 0.5$ and $g_{12} = -1.95$.

role played by the interatomic interactions as we clearly showed the MI features to be very sensitive to their variations and signs. Most importantly, the fact that soliton molecules are generated through the activation of MI demonstrates the exclusivity of the proposed modified model and the accuracy of our predictions.

The soliton interaction is a problem of fundamental importance in the propagation dynamics of any nonlinear media. In the context of Bose-Einstein condensates, an experiment on the formation and propagation of matter-wave soliton trains has been reported and found that, even though the interatomic interactions are attractive, the neighboring solitons repel each other with a force that is dependent on their separation [73]. The interaction potential between two solitons due to their phases has been investigated using the symmetric and antisymmetric combinations of the Gaussian wave functions of a single soliton to represent the soliton train with alternating phases, which can be generated by quantum mechanical phase fluctuations of the bosonic field operator. It has been confirmed that the source of the repulsive force is a phase difference of π between two neighboring solitons [74]. By using an effective one-dimensional time-dependent non-polynomial nonlinear Schrödinger equation, the scattering of bright solitons in a Bose-Einstein condensate induced by a sudden change in the sign of the scattering length from positive to negative, leading to a shift in the position of fringes and the conditions for their collapse at the collision have been studied. In particular, by changing the phase difference by π , the spatial locations of the maxima of interference are shifted into the minima positions [75]. Indeed, a novel phenomenon, namely, the intermittent dynamics of individual peaks during the time evolution of the soliton train in an axial harmonic potential, has been found [76]. The collisional dynamics of matter-wave solitons, which depend on the relative phase between the solitons, have been explored using real-time imaging. It has been observed that in-phase collisions sometimes result in the destruction or fusion of the soliton pair. In contrast, out-of-phase collisions are incredibly robust against collapse and survive many oscillations in the trap [77].

Naively, questions may be arising whether the objects obtained in Fig. 8-12 are solitons, which is a legitimate question when it comes to systems like the one understudy, which may also support the appearance of quantum droplets, which do not necessarily depend on the integrability of system (6) broken by the presence of interatomic interaction terms, the SO coupling, and the BMF terms. Moreover, the simulations from Figs. 8(b) and 9(b) already give some flavors of wave interaction which, if deeply conducted, will confirm whether our results are indeed train of solitons. To this end, it would be of interest to precise that beyond the activation of MI of cw, other methods have been used in the meantime to induce soliton train in cold atom systems, and Bose-Einstein condensates, in particular, the main aim being to reproduce results from the seminal experiment by Strecker et al. [73] on a condensate of ^{7}Li atoms using Feshbach resonance. Quantum mechanical phase fluctuations of the bosonic field operator were recently proposed to activate the formation of trains of solitons, where Al Khawaja et al. [74] have reproduced the appearance of the soliton train in the 1D time-dependent GP equation by adopting a suitable space-dependent pattern in the initial phase of the Bose-Einstein condensate. The dynamical process underlying soliton train formation induced by MI using the time-dependent GP equation in the presence of a three-body dissipative term was explained and numerically tested using the ansatz $\psi(x) = f_0[f(x-x_0) + f(x+x_0)e^{i\Delta\phi}]$, with $\Delta\phi$ being the phase difference of two neighboring bright solitons centered in $-x_0$ and x_0 and $f_0 = 1/\sqrt{2}$. Applying a similar ansatz to the system at hand, one obtains the results in Figs. 13 and 14 for $\Delta\phi = 0$ and $\pi/2$, respectively. Obviously, from the initial states of the two-soliton ansatz displayed in Figs. 13(a1) and (b1), where $\Delta\phi = 0$, the multiple interactions of the two entities generate trains of solitonic objects that are a true signature of the MI phenomenon. With the effect of the sign of the helicoidal gauge potential, there is delocalization of the wave packet, showing the difference that was already noticed in Fig. 12. Initially, the two solitons are attractive, and their interaction gives rise to a static peak which radiates some small solitons and gets involved into multiple collisions to generate what is observed in Figs. 13(a1) and (b1). This takes place in the whole space, but with increasing time, although no physical trap is set, the SO effect brings about some trapping effect, which is part of its consequences. Soliton trains occurrence also takes place for $\Delta\phi = \pi/2$ as depicted in Fig. 14, where the same conditions as in Fig. 13 have been considered. The effectiveness of our predictions is further tested by com-

paring results for $\Delta\phi = 0$ and $\Delta\phi = \pi$ in Fig. 15. It is, in fact, shown that the densities in the two cases are inverted, but still, the robustness of the formed structures is confirmed, which consolidates our numerical simulations. The fringes result from self-interference of small radiations, which further supports that the structures observed in our previous MI long-time simulation are solitons. Indeed, we suspect the vital aspects that govern wave collision in Bose-Einstein condensate not to be exhaustively true for the case at hand because of the absence of potential on the one hand and the presence of the LHY terms and SO coupling on the other hand. However, we believe that some other aspects and governing rules may be explored that are specific to the beyond MF formulation of BB mixtures and which accommodate the helicoidal SO or any different type of SO coupling. Interestingly, the left- and right-handed helicoidal gauge reveals the versatility of the model proposed in the present work, which may importantly affect the effect brought by the phase difference in the process of MI induced by wave-wave interaction.

IV. CONCLUSION

The primary purpose of this paper was the study of the input of the helicoidal SO coupling in the emergence of MI in Bose-Bose mixtures through coupled GP equations containing LHY terms. The linear stability analysis of cws has been utilized to find an expression for the MI growth rate, and discuss regions of parameters likely to give rise to droplet-like states. This has been conducted via a comprehensive parametric study of the growth rate, which has been found to be very sensitive to changes in not only the interatomic interactions but also helicoidal SO components. For example, with increasing the helicoidal gauge potential, separated regions of instability tend to merge and form a unique instability area in the context where the intercomponent interactions are attractive, and the intracomponent interactions are repulsive. Additionally, in the instability $(\alpha, \beta)-$phase plane of the growth rate, repulsive intracomponent interactions expand the instability region. Analytical results have been confronted to direct numerical simulations on the modified model. In general, trains of solitonic objects have been obtained under a suitable choice of parameters, with a strong dependence on the helicoidal gauge potential and the SO coupling strength. The spatial profiles of the obtained structures reveal the instability to generate soliton molecules whose topology and characteristics depend highly on the interatomic interactions and the helicoidal SO coupling, which can be left- or right-handed. This gives credit to the model used and the technique of MI, which is universally known as a natural precursor to the formation of nonlinear patterns and soliton trains as it typically occurs in the same parameter region where solitons are observed.

The relationship between key parameters of a one-dimensional Bose mixture was recently discussed, and exact quantum droplet solutions were found [42, 78]. Further contribution in that direction showed that the same context could be adopted for quantum droplets to be obtained under the activation of MI. That was confirmed via direct numerical simulations. One of the urgent new directions to be given to this work is finding regions of parameters where droplets can be obtained as exact solutions or under the activation of MI, including the new condition brought by the presence of the helicoidal SO coupling. The study may be extended to its two- and three-dimensional formulations in order to explore more elaborated and composite structures.

ACKNOWLEDGMENTS

The work by CBT is supported by the Botswana International University of Science and Technology under the grant **DVC/RDI/2/1/16I (25)**. CBT thanks the Kavli Institute for Theoretical Physics (KITP), University of California Santa Barbara (USA), where this work was supported in part by the National Science Foundation Grant no.**NSF PHY-1748958**, NIH Grant no.**R25GM067110**, and the Gordon and Betty Moore Foundation Grant no.**2919.01**.

[1] F. Lederer, G. I. Stegeman, D. N. Christodoulides, G. Assanto, M. Segev, and Y. Silberberg, Phys. Rep. **463**, 1 (2008).
[2] J. W. Miles, Ann. Rev. Fluid Mech. **12**, 11 (1980).
[3] R. Rajaraman, *Solitons and Instantons*, (North-Holland, Amster- dam, 1987).
[4] R. Ichiki, S. Yoshimura, T. Watanabe, Y. Nakamura and Y. Kawai, Phys. Plasmas **9**, 4481 (2002).
[5] C. S. Panguetna, C. B. Tabi, and T. C. Kofané, Phys. Plasmas **24**, 092114 (2017).
[6] C. S. Panguetna, C. B. Tabi and T. C. Kofané, Commun. Nonl. Sci. Numer. Simulat. **55**, 326 (2018).
[7] J. B. Okaly, A. Mvogo, C. B. Tabi, H. P. Ekobena Fouda and T. C. Kofané, Phys. Rev. E **102**, 062402 (2020).
[8] J. B. Okaly, F. II Ndzana, R. L. Woulaché, C. B. Tabi and T. C. Kofané, Chaos **29**, 093103 (2019).
[9] C. B. Tabi, R. Y. Ondoua, H. P.Ekobena Fouda and T. C. Kofané, Phys. Lett. A **380**, 2374 (2016).
[10] L. Pitaevski and S. Stringari, *Bose-Einstein Condensation and Superfluidity*, (Oxford University Press, Oxford, 2016).
[11] T. B. Benjamin and J. E. Feir, J. Fluid Mech. **27**, 417 (1967).
[12] L. A. Ostrovskii, Sov. Phys. JETP **24**, 797 (1967).
[13] A. Hasegawa and F. Tappert, Appl. Phys. Lett. **23**, 142 (1973).

[14] F. II Ndzana, A. Mohamadou, and T. C. Kofané, Chaos **18**, 043121 (2008).
[15] E. Kengne, A. Lakhssassi, W. M. Lui, and R. Vaillancourt, Phys. Rev. E **87**, 022914 (2013).
[16] L. T. Megne, C. B. Tabi and T. C. Kofané, Phys. Rev. E **102**, 042207 (2020).
[17] C. B. Tabi, J. Phys.: Cond. Matter **22**, 414107 (2010).
[18] I. Maïna, C. B. Tabi, H. P. Ekobena Fouda , A. Mohamadou and T. C. Kofané, Chaos **25**, 043118 (2015).
[19] C. B. Tabi, A. S. Etémé, A. Mohamadou and T. C. Kofané, Chaos Solit. Fract. **123**, 116 (2019).
[20] G. R. Mefire Yone, C. B. Tabi, A. Mohamadou, H. P. Ekobena Fouda and T. C. Kofané, Chaos **23**, 033128 (2013).
[21] C. D. K. Bansi, C. B. Tabi and A. Mohamadou, Chaos Solit. Fract. **109**, 170 (2018).
[22] R. Gupta, T. S. Raju, C. N. Kumar and P. K. Panigrahi, J. Opt. Soc. Am. B **29**, 3360 (2012).
[23] V. K. Sharma, A. Goyal, T. S. Raju, C. N. Kumar and P. K. Panigrahi, Opt. Fiber Technol. **24**, 119 (2015).
[24] D. S. Petrov, Phys. Rev. Lett. **115**, 155302 (2015).
[25] G. Semeghini, G. Ferioli, L. Masi, C. Mazzinghi, L. Wolswijk, F. Minardi, M. Modugno, G. Modugno, M. Inguscio, and M. Fattori, Phys. Rev. Lett. **120**, 235301 (2018).
[26] F. Wächtler and L. Santos, Phys. Rev. A **93**, 061603(R) (2016).
[27] D. Baillie, R. M. Wilson, R. N. Bisset, and P. B. Blakie, Phys. Rev. A **94**, 021602(R) (2016).
[28] R. N. Bisset, R. M. Wilson, D. Baillie, and P. B. Blakie, Phys. Rev. A **94**, 033619 (2016).
[29] T. D. Lee, K. Huang, and C. N. Yang, Phys. Rev. **106**, 1135 (1957).
[30] O. Gessner and A. F. Vilesov, Ann. Revi. Phys. Chem. **70**, 173 (2019).
[31] F. Laimer, L. Kranabetter, L. Tiefenthaler, S. Albertini, F. Zappa, A. M. Ellis, M. Gatchell, and P. Scheier, Phys. Rev. Lett. **123**, 165301 (2019).
[32] Y. V. Kartashov, G. E. Astrakharchik, B. A. Malomed, and L. Torner, Nat. Rev. Phys. **1**, 185 (2019).
[33] I. Ferrier-Barbut, H. Kadau, M. Schmitt, M. Wenzel, and T. Pfau, Phys. Rev. Lett. **116**, 215301 (2016).
[34] L. Chomaz, S. Baier, D. Petter, M. J. Mark, F. Wächtler, L. Santos, and F. Ferlaino, Phys. Rev. X **6**, 041039 (2016).
[35] C. R. Cabrera, L. Tanzi, J. Sanz, B. Naylor, P. Thomas, P. Cheiney, and L. Tarruell, Science **359**, 301 (2018).
[36] P. Cheiney, C. R. Cabrera, J. Sanz, B. Naylor, L. Tanzi, and L. Tarruell, Phys. Rev. Lett. **120**, 135301 (2018).
[37] I. Ferrier-Barbut, Phys. Today **72**, 46 (2019).
[38] G. Ferioli, G. Semeghini, L. Masi, G. Giusti, G. Modugno, M. Inguscio, A. Gallemi, A, Recati, and M. Fattori, Phys. Rev. Lett. **122**, 090401 (2019).
[39] H. Kadau, M. Schmitt, M. Wenzel, C. Wink, T. Maier, I. Ferrier- Barbut and T. Pfau, Nature **530**, 194 (2016).
[40] Y. Tang, N. Q. Burdick, K. Baumann, and B. L. Lev, New J. Phys.**17**, 045006 (2015).
[41] M. Schmitt, M. Wenzel, F. Böttcher, I. Ferrier-Barbut, and T. Pfau, Nature (London) **539**, 259 (2016).
[42] D. S. Petrov and G. E. Astrakharchik, Phys. Rev. Lett. **117**, 100401 (2016).
[43] Y.-J. Lin, K. Jiménez-García, and I. B. Spielman, Nature (London) **471**, 83 (2011).
[44] Y.-J. Lin, R. L. Compton, K. Jiménez-Garcia, W. D. Phillips, J. V. Porto, and I. B. Spielman, Nat. Phys. **7**, 531 (2011).
[45] R. A. Williams, M. C. Beeler, L. J. LeBlanc, K. Jimenez-Garcia, and I. B. Spielman, Phys. Rev. Lett. **111**, 095301 (2013).
[46] P. Wang, Z.-Q. Yu, Z. Fu, J. Miao, L. Huang, S. Chai, H. Zhai, and J. Zhang, Phys. Rev. Lett. **109**, 095301 (2012).
[47] L. Huang, Z. Meng, P. Wang, P. Peng, S.-L. Zhang, L. Chen, D. Li, Q. Zhou, and J. Zhang, Nat. Phys. **12**, 540 (2016).
[48] Z. Meng, L. Huang, P. Peng, D. Li, L. Chen, Y. Xu, C. Zhang, P. Wang, and J. Zhang, Phys. Rev. Lett. **117**, 235304 (2016).
[49] I. A. Bhat, T. Mithun, B. A. Malomed, and K. Porsezian, Phys. Rev. A **92**, 063606 (2015).
[50] S. Bhuvaneswari, K. Nithyanandan, P. Muruganandam, and K. Porsezian, J. Phys. B **49**, 245301 (2016).
[51] T. Mithun and K. Kasamatsu, J. Phys. B: At. Mol. Opt. Phys. **52**, 045301 (2019).
[52] V. E. Lobanov, Y. V. Kartashov, and V. V. Konotop, Phys. Rev. Lett. **112**, 180403 (2014).
[53] H. Sakaguchi, B. Li, and B. Malomed, Phys. Rev. E **89**, 032920 (2014).
[54] A. Tononi, Y. Wang, and L. Salasnich, Phys. Rev. A **99**, 063618 (2019).
[55] D. Singh, M. K Parit, T. S. Raju and P. K Panigrahi, J. Phys. B: At. Mol. Opt. Phys. **53**, 245001 (2020).
[56] Y. V. Kartashov and V. V. Konotop, Phys. Rev. Lett. **118**, 190401 (2017).
[57] M. C. Rechtsman, J. M. Zeuner, Y. Plotnik, Y. Lumer, D. Podolsky, F. Dreisow, S. Nolte, M. Segev, and A. Szameit, Nature (London) **496**, 196 (2013).
[58] X.-X. Li, R.-J. Cheng, A.-X. Zhang, and J.-K. Xue, Phys. Rev. E **100**, 032220 (2019).
[59] P. Otlaadisa, C. B. Tabi and T. C. Kofané, Phys. Rev. E **103**, 052206 (2021)
[60] M. C. Rechtsman, J. M. Zeuner, Y. Plotnik, Y. Lumer, D. Podolsky, F. Dreisow, S. Nolte, M. Segev, and A. Szameit, Nature (London) **496**, 196 (2013).
[61] S. V. Samsonov, A. D. R. Phelps, V. L. Bratman, G. Burt, G. G. Denisov, A. W. Cross, K. Ronald, W. He, and H. Yin, Phys. Rev. Lett. **92**, 118301 (2004).
[62] D. M. Larsen, Ann. Phys., NY **24**, 89 (1963)
[63] B. Oleś, and K. Sacha, J. Phys. A: Math. Theor. **41**, 145005 (2008).
[64] K. Lakomy, R. Nath, and L. Santos, Phys. Rev. A **86**, 013610 (2012).
[65] B. B. Baizakov, S. M. Al-Marzoug, and H. Bahlouli, Phys. Rev. A **92**, 033605 (2015).
[66] B. B. Baizakov, S. M. Al-Marzoug, U. Al Khawaja, and H. Bahlouli, J. Phys. B **52**, 095301 (2019).
[67] A. V. Buryak and N. N. Akhmediev, Phys. Rev. E **51**, 3572 (1995).
[68] B. A. Malomed, Phys. Rev. E **47**, 2874 (1993).
[69] A. Zavyalov, R. Iliew, O. Egorov, and F. Lederer, Phys. Rev. A **80**, 043829 (2009).
[70] N. N. Akhmediev, A. Ankiewicz, and J. M. Soto-Crespo, Phys. Rev. Lett. **79**, 4047 (1997).
[71] M. Haelterman, S. Trillo, and P. Ferro, Opt. Lett. **22**, 84 (1997).
[72] S. K. Adhikari, Phys. Rev. A **100**, 063618 (2019).
[73] K. E. Strecker, G. B. Partridge, A. G. Truscott, and R. G. Hulet, Nature (London) **417**, 150 (2002).
[74] U. Al Khawaja, H. T. C. Stoof, R. G. Hulet, K. E. Strecker, and G. B. Partridge, Phys. Rev. Lett. **89**,

200404 (2002).
[75] L. Salasnich, A. Parola, and L. Reatto, Phys. Rev. A **66**, 043603 (2002).
[76] L. Salasnich, A. Parola, and L. Reatto, Phys. Rev. Lett. **91**, 080405 (2003).
[77] J H. V. Nguyen, P. Dyke, D. Luo, B. A. Malomed and R. G. Hulet, Nature Phys. **10**, 918 (2014).
[78] T. Mithun, A. Maluckov, K. Kasamatsu, B. A. Malomed, and A. Khare, Symmetry **12**, 174 (2020)